1-1-2013

Microstructural origin for the piezoelectricity evolution in (K0.5Na0.5)NbO3-based lead-free ceramics

Hanzheng Guo
Iowa State University

Shujun Zhang
The Pennsylvania State University, shujun@uow.edu.au

Scott P. Beckman
Iowa State University

Xiaoli Tan
Iowa State University

Microstructural origin for the piezoelectricity evolution in (K0.5Na0.5)NbO3-based lead-free ceramics

Abstract

Chemically modified (K0.5Na0.5)NbO3 compositions with finely tuned polymorphic phase boundaries (PPBs) have shown excellent piezoelectric properties. The evolution of the domain morphology and crystal structure under applied electric fields of a model material, 0.948(K0.5Na0.5)NbO3-0.052LiSbO3, was directly visualized using in situ transmission electron microscopy. The in situ observations correlate extremely well with measurements of the electromechanical response on bulk samples. It is found that the origin of the excellent piezoelectric performance in this lead-free composition is due to a tilted monoclinic phase that emerges from the PPB when poling fields greater than 14 kV/cm are applied. 2013 AIP Publishing LLC.

Keywords

lead, nbo3, 5, evolution, microstructural, 5na0, origin, piezoelectricity, ceramics, free, k0

Disciplines

Engineering | Physical Sciences and Mathematics

Publication Details

Guo, H., Zhang, S., Beckman, S. P. & Tan, X. (2013). Microstructural origin for the piezoelectricity evolution in (K0.5Na0.5)NbO3-based lead-free ceramics. Journal of Applied Physics, 114 (15), 154102-1-154102-8.

AIP Journal of Applied Physics

Microstructural origin for the piezoelectricity evolution in (K0.5Na0.5)NbO3-based lead-free ceramics

Hanzheng Guo, Shujun Zhang, Scott P. Beckman, and Xiaoli Tan

Citation: Journal of Applied Physics **114**, 154102 (2013); doi: 10.1063/1.4825213
View online: http://dx.doi.org/10.1063/1.4825213
View Table of Contents: http://scitation.aip.org/content/aip/journal/jap/114/15?ver=pdfcov
Published by the AIP Publishing

Microstructural origin for the piezoelectricity evolution in $(K_{0.5}Na_{0.5})NbO_3$-based lead-free ceramics

Hanzheng Guo,[1] Shujun Zhang,[2] Scott P. Beckman,[1] and Xiaoli Tan[1,a)]
[1]*Department of Materials Science and Engineering, Iowa State University, Ames, Iowa 50011, USA*
[2]*Materials Research Institute, Pennsylvania State University, University Park, Pennsylvania 16802, USA*

(Received 19 July 2013; accepted 30 September 2013; published online 15 October 2013)

Chemically modified $(K_{0.5}Na_{0.5})NbO_3$ compositions with finely tuned polymorphic phase boundaries (PPBs) have shown excellent piezoelectric properties. The evolution of the domain morphology and crystal structure under applied electric fields of a model material, $0.948(K_{0.5}Na_{0.5})NbO_3$–$0.052LiSbO_3$, was directly visualized using *in situ* transmission electron microscopy. The *in situ* observations correlate extremely well with measurements of the electromechanical response on bulk samples. It is found that the origin of the excellent piezoelectric performance in this lead-free composition is due to a tilted monoclinic phase that emerges from the PPB when poling fields greater than 14 kV/cm are applied. © *2013 AIP Publishing LLC*. [http://dx.doi.org/10.1063/1.4825213]

I. INTRODUCTION

Piezoelectric materials are crucial in numerous important applications and are the foundation of a multibillion dollar industry.[1,2] For over half a century, the principle piezoelectric materials used in engineering technologies have been based on $Pb(Zr,Ti)O_3$;[3] however, the toxicity of lead is a significant problem, and recent legislations have been enacted that restrict the use of lead-based compounds.[4] One of the most promising alternatives is the $(K_{0.5}Na_{0.5})NbO_3$ (KNN)-based solid solution system.[5–11] Various chemical modifiers, such as $LiTaO_3$,[12,13] $LiNbO_3$,[14–16] and $LiSbO_3$,[17,18] have been employed to facilitate processing and optimize the piezoelectric behavior. The enhanced piezoelectricity in these compositionally modified KNN-based oxides is a result of reducing the temperature of the polymorphic phase boundary (PPB), where the tetragonal and orthorhombic phases coexist, from ~210 °C, for unmodified KNN, to near room temperature.[5]

The physical mechanism for the piezoelectric activity in these KNN-based oxides, particularly those with a PPB near room temperature, has only recently been investigated. Observations from conventional transmission electron microscopy (TEM) attribute the enhanced piezoelectricity to the existence of nanodomains of mixed tetragonal and orthorhombic phases in the virgin state.[19] However, for originally isotropic polycrystalline ferroelectrics, the piezoelectricity is imparted through a poling process, where a strong direct current electric field is applied to develop a polar symmetry (∞m) by spontaneous polarization alignment in the form of ferroelectric domain switching.[20] Recent X-ray diffraction on bulk samples of KNN-based ceramics during electrical poling indicate that, in addition to domain switching, phase transitions have also been observed.[21–23] Presumably, the nanodomains do not survive the poling process, which raises questions about their relevance.

It has been known that domains and crystal structures dictate the physical properties of ferroelectric crystals. Therefore, the evolution of ferroelectric domain and phase symmetry under a poling field is key to understanding the microstructural origin of the piezoelectricity development at the PPB. Such information requires *in situ* TEM study and is still missing from literature for KNN-based piezoelectrics. In a recent study on the $(1\text{-}x)(Bi_{1/2}Na_{1/2})TiO_3$–$xBaTiO_3$ (BNT–BT) system, we have directly observed, via electric field *in situ* TEM, that the poling process can destroy morphotropic phase boundaries (MPBs) as well as create new MPBs from a single phase region.[24] The poling-created MPB is responsible for the enhanced piezoelectricity.[24] In contrast to BNT–BT, the best piezoelectric properties in KNN-based ceramics are observed in the PPB compositions. To uncover the microstructural mechanism responsible for the enhanced piezoelectricity, several critical questions need to be answered: Does the PPB survive electrical poling? How do the domain morphology and the crystal structure change? Do these changes correlate with the macroscopic piezoelectricity?

In this study, the ferroelectric domain morphology and crystal symmetry are simultaneously monitored in real time during poling with an electric field *in situ* TEM technique.[25–29] The PPB composition of $0.948(K_{0.5}Na_{0.5})NbO_3$–$0.052LiSbO_3$ (KNN-5.2LS) is studied because its structure (mixed tetragonal and orthorhombic phases) and piezoelectric response ($d_{33} \sim 265$ pC/N) are representative of KNN-based piezoelectrics.[17,18] The *in situ* observations are combined with the corresponding dielectric, piezoelectric, and *ex situ* X-ray diffraction measurements to determine the microstructural origin of the piezoelectricity evolution at the PPB in KNN-based piezoelectrics.

II. EXPERIMENTAL DETAILS

The solid state reaction method was used to prepare the $0.948(K_{0.5}Na_{0.5})NbO_3$–$0.052LiSbO_3$ ceramic, with K_2CO_3 (99.5%), Na_2CO_3 (99.8%), Li_2CO_3 (99.9%), Nb_2O_5 (99.5%), and Sb_2O_5 (99.9%) as starting materials. All the raw powders

a)Author to whom correspondence should be addressed. Electronic mail: xtan@iastate.edu

were dried at 200 °C and subsequently weighed according to the formulation. The powders were milled in anhydrous ethanol for 24 h and then calcined at 880 °C for 2 h. The calcined powders were once again milled, and 3 wt. % binder was added to the dried powder. Granulated powder was pressed into pellets 12 mm in diameter. The binder was removed at 600 °C, followed by sintering at 1100 °C for 2 h in air. After sintering, hot isostatic pressing at 21 MPa and 1000 °C for 2 h was carried out in an argon atmosphere with 2% oxygen.

For piezoelectric characterization, silver films were sputtered onto the pellet to serve as electrodes. The ceramic specimens were poled at a series of electric fields at room temperature (25 °C) for 10 min. The piezoelectric coefficient d_{33} was measured with a piezo-d_{33} meter (ZJ-4B, Institute of Acoustics, Chinese Academy of Sciences) 24 h after poling. For dielectric properties measurements, silver paste (Dupont 6160) was fired on at 750 °C for 6 min as electrodes. Dielectric properties were measured immediately after room-temperature poling during separate heating and cooling processes. The measurement upon heating was carried out using an LCR meter (HP-4284A, Hewlett-Packard) in a tube furnace at a rate of 4 °C/min. Measurements below room temperature were carried out during continuous cooling with liquid N_2 at the same rate with an LCZ meter (Keithley 3330) in conjunction with a temperature chamber.

For *ex situ* X-ray diffraction measurements, conductive epoxy was applied on the polished surfaces and then removed chemically with acetone after poling. The whole diffraction spectra were recorded with a Siemens D500 diffractometer using Cu-Kα radiation at a 0.05° step size and a 1 second per step dwell time. To monitor the development of the 1/2(103) superlattice peak, the dwell time per step was 150 s.

For electric field *in situ* TEM experiments, disk specimens (3 mm in diameter) were prepared from as-processed pellets through standard procedures including grinding, cutting, dimpling, and ion milling. The dimpled disks were annealed at 400 °C for 2 h to minimize the residual stresses before Ar-ion milling to the point of electron transparency. *In situ* TEM experiments were carried out on a specimen that was crack free at the edge of the central perforation on a Phillips CM30 microscope operated at 200 kV. The presence of a central perforation intensified the electric field in the TEM specimen. This intensification ratio is 2 for an ideal circular perforation.[27] The electric fields quoted in the text and figure captions for the *in situ* TEM results are double of the nominal fields.

III. RESULTS AND DISCUSSION

A. Electric field *in situ* TEM study

Three nearby grains in one TEM specimen were focused along their [111], [110], and [001] zone axes, respectively. Fig. 1 shows the results from the [111]-aligned grain, where

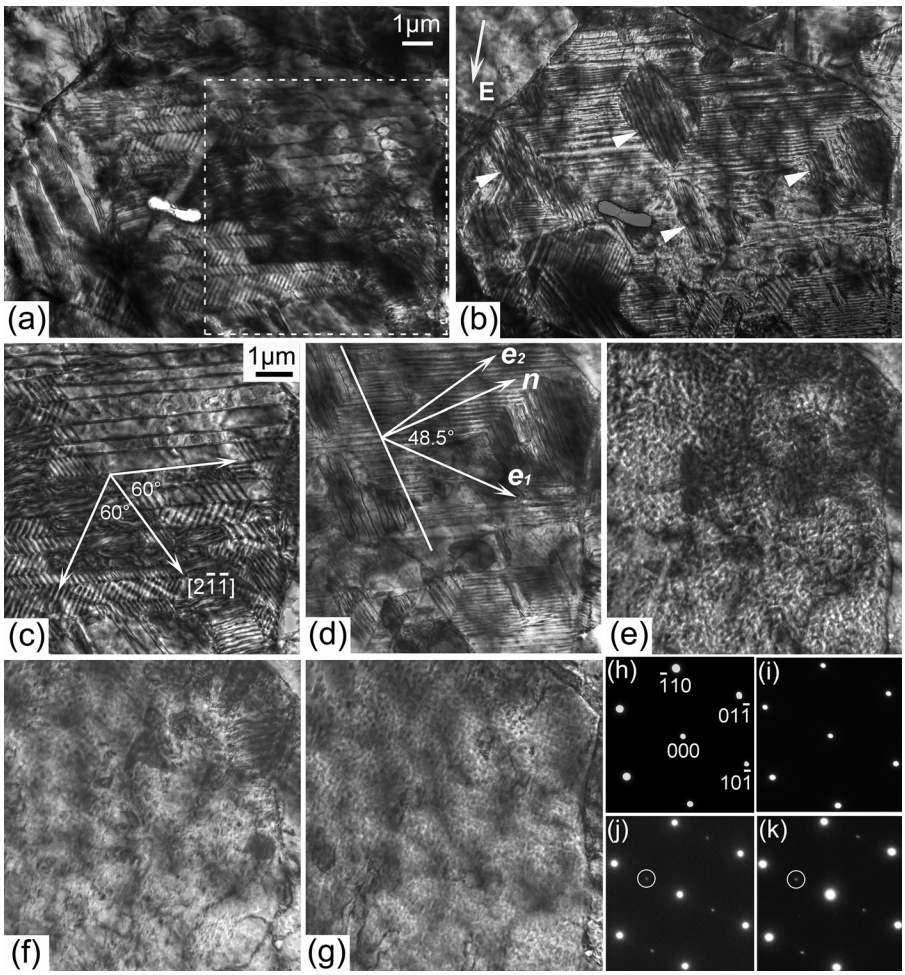

FIG. 1. *In situ* TEM observations of a grain along the [111] zone axis in a KNN-5.2LS specimen during electrical poling. Bright-field micrographs at (a) virgin state, and (b) 8 kV/cm are displayed to show almost the entire grain. The direction of poling fields is indicated by the bright arrow in (b). The area in the dashed box in (a) is focused for further illustration at (c) virgin state, (d) 8 kV/cm, (e) 14 kV/cm, (f) 22 kV/cm, and (g) 24 kV/cm. Representative selected area diffraction patterns recorded at (h) virgin state, (i) 8 kV/cm, (j) 14 kV/cm, and (k) 24 kV/cm are displayed, with 1/2{*oeo*} superlattice diffraction spots highlighted by bright circles.

Figs. 1(a) and 1(b) are the overview of almost the entire grain in the virgin state and at 8 kV/cm, respectively. The dashed area in Fig. 1(a) was further focused. In the virgin state (Figs. 1(a) and 1(c)), most domains are found to form the typical herringbone morphology, which is a common pattern in unpoled $BaTiO_3$ ceramics,[30] unmodified KNN ceramics,[31] as well as KNN-based PPB compositions.[19,32] The herringbone pattern contains parallel strips less than 1 μm in width, several to tens of μm in length, and a substructure of narrow V-shaped domains. Within most of the herringbone strips, parallel short lamellar domains with alternating bright and dark contrast are present. The V-shape forms a 120° angle and is bisected by the long domain wall. Both walls for the short lamellar domains and the long domains are found along the $\langle 2\bar{1}\,\bar{1}\rangle$ directions (Fig. 1(c)). With assistance from a [111] stereographic projection map, these edge-on domain walls are determined to be on the $\{01\bar{1}\}$ planes. In addition to the herringbone pattern, another type of domain morphology with broader width ($\sim$1 μm) and inclined domain walls (referred to as broad strips) are found at the left corner of the grain (Fig. 1(a)). Under the poling field of 8 kV/cm, the short lamellar domains in the herringbone pattern disappear, and the long domains become much narrower (Fig. 1(b)). Additionally, islands of another set of lamellar domains (indicated by bright triangles in Fig. 1(b)), whose domain walls are inclined and parallel to that of the original broad strips in Fig. 1(a), are observed. The normal $\boldsymbol{n}$ to the trace of these domain walls is found to be about 48.5° from $[10\bar{1}]$ ($\boldsymbol{e_1}$ in Fig. 1(d)) and 11.5° from $[01\bar{1}]$ ($\boldsymbol{e_2}$ in Fig. 1(d)). Crystallographic analysis indicates that the domain walls of the broad strips in the virgin state (left corner of the grain in Fig. 1(a)) and those in the isolated islands at 8 kV/cm (Fig. 1(b)) are most likely on the $\{12\bar{1}\}$ planes. Increasing the poling field from 8 to 24 kV/cm leads to the disruption of the μm-sized lamellar domains to sub-μm-sized features (100–200 nm) and eventually to a new domain morphology with nano-sized blotches (referred to as blotchy domains). Fig. 1(e) shows the domain morphology at 14 kV/cm, where some hints of the original μm-sized lamellar domains can still be found. The lamellar domains continue transforming to blotchy domains with increasing field (Fig. 1(f)) and eventually completely disappear at 24 kV/cm (Fig. 1(g)).

The evolution of the corresponding selected area electron diffraction pattern (EDP) is displayed in Figs. 1(h)–1(k). The EDP recorded at 8 kV/cm (Fig. 1(i)) stays the same as the virgin state (Fig. 1(h)). However, it is interesting to notice that one set of 1/2{*oeo*} (*o* and *e* stand for the odd and even Miller indices, respectively) superlattice diffraction spots (one is highlighted by a bright circle) is observed at 14 kV/cm (Fig. 1(j)). This is the poling field where the blotchy domains start to appear (Fig. 1(e)). Further increasing the poling field to 24 kV/cm preserves the superlattice spots (Fig. 1(k)). It is known that the PPB composition in the virgin state of KNN-based ceramics is a mixture of orthorhombic (space group *Amm2*) and tetragonal (space group *P4mm*) phases,[15,16] both of which do not show any superlattice diffraction spots. Therefore, the appearance of 1/2{*oeo*} superlattice diffraction spots certainly reveals an electric field-induced oxygen octahedra tilting at 14 kV/cm and beyond.

Fig. 2 shows the microstructural responses to poling fields in another grain recorded along its [110] zone axis. In

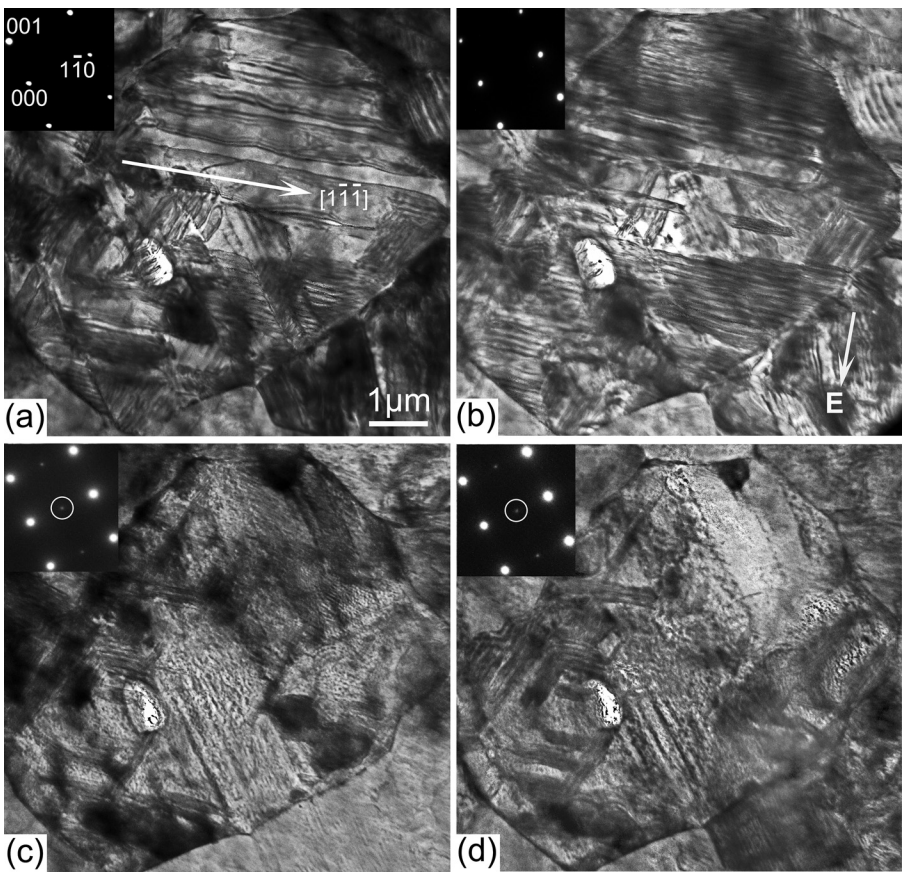

FIG. 2. *In situ* TEM observations of a near-by grain along the [110] zone axis in the same KNN-5.2LS specimen as examined in Fig. 1 during electrical poling. Bright-field micrographs at (a) virgin state, (b) 8 kV/cm, (c) 14 kV/cm, and (d) 24 kV/cm are displayed. The direction of poling fields is indicated by the bright arrow in (b). Representative selected area diffraction patterns at each poling field are shown in the insets, with 1/2{*oeo*} superlattice diffraction spots indicated by bright circles.

the virgin state, the broad strips with inclined domain walls along the $[1\bar{1}\bar{1}]$ direction occupy the upper half of the grain (Fig. 2(a)). The typical herringbone domains are found in the lower half with two sets of short lamellar domains along two $\langle 1\bar{1}1\rangle$ directions. Crystallographic analysis using the [110] stereographic projection map indicates the walls of the lamellar domains in the herringbone structure are on the $\{01\bar{1}\}$ planes. The domain walls of the broad strips are verified to be along the $\{12\bar{1}\}$ planes, which is consistent with the results for the [111] zone axis shown in Fig. 1. Again, the herringbone type domains are transformed to μm-sized long lamellar domains at 8 kV/cm (Fig. 2(b)) without any noticeable change in EDP (shown in the insets). Figs. 2(a) and 2(b) seem to suggest that the domains with $\{12\bar{1}\}$ walls change to those with $\{01\bar{1}\}$ walls under low poling fields. Similar changes are also observed in Figs. 1(a) and 1(b) along the [111] zone axis. Therefore, the walls of the lamellar domains observed at 8 kV/cm may be on either the $\{01\bar{1}\}$ planes, the $\{12\bar{1}\}$ planes, or a mixture of the two. Further increase in the poling field to 14 kV/cm leads to the appearance of the 1/2*{oeo}* superlattice diffraction spots and blotchy domains (Fig. 2(c)), and these features remain at 24 kV/cm (Fig. 2(d)). It should be noted that the formation of a microcrack was observed very close to this grain at 24 kV/cm. This may have diluted the electric field in this grain, and hence only slight changes in domain morphology are observed from 14 to 24 kV/cm. However, most of the grain is transformed to blotchy domains, which is accompanied by the presence of 1/2*{oeo}* superlattice diffraction spots.

Fig. 3 shows another scenario along the [001] zone axis. Similar responses to the poling field are observed again. In the virgin state, herringbones are found with the intersecting line along the [010] direction (Fig. 3(a)). Within the herringbone bands, parallel and perpendicular lamellar domains are observed. At 8 kV/cm, the whole grain is occupied by two sets of thin, long lamellar domains along two $\langle 110\rangle$ directions (Fig. 3(b)). Slightly increasing the poling field to 10 kV/cm results in one set of the lamellar domains disappearing. Nearly half of the grain is transformed to μm-sized rectangular blocks that have slightly curved boundaries roughly along two $\langle 100\rangle$ directions (Fig. 3(c)). Crystallographic analysis indicates that these inclined boundaries are most likely on the (011) and (101) planes. The lamellar domains completely disappear at 14 kV/cm, and the entire grain adopts the rectangular structure (Fig. 3(d)). It should be pointed out that this occurs at the same poling field where the blotchy domains and the 1/2*{oeo}* superlattice spots appear in the other two grains. When the field is further increased to 18 kV/cm, one set of the inclined boundaries disappears and the blotchy domains become apparent and uniform (Fig. 3(e)). At 24 kV/cm, the second set of inclined boundaries also disappears, and small blotchy domains as well as large dark patches with diffused contrast are seen (Fig. 3(f)). However, the EDP always stays unchanged from the virgin state with no 1/2*{oeo}* superlattice spots. This might be due to the fact that the oxygen octahedra tilting axis is perpendicular to the [001] zone axis and is invisible under this configuration.[33]

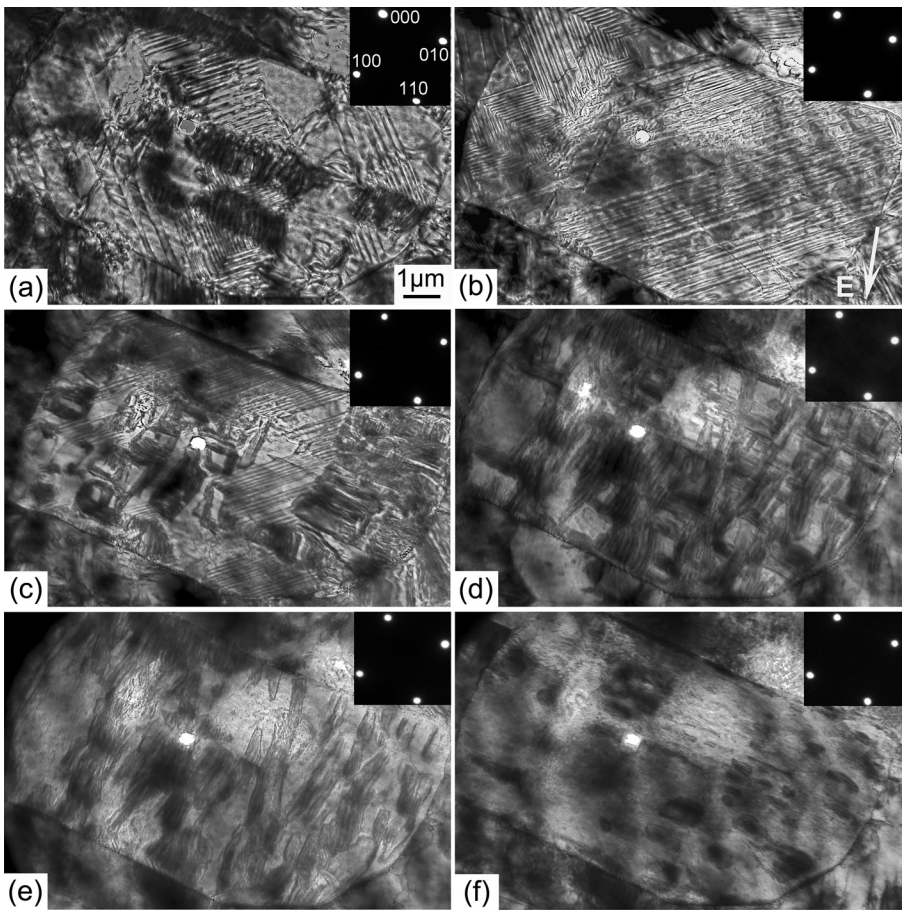

FIG. 3. *In situ* TEM observations of a near-by grain along the [001] zone axis in the same KNN-5.2LS specimen as examined in Fig. 1 during electrical poling. Bright-field micrographs at (a) virgin state, (b) 8 kV/cm, (c) 10 kV/cm, (d) 14 kV/cm, (e) 18 kV/cm, and (f) 24 kV/cm are displayed. The direction of poling fields is indicated by the bright arrow in (b). Representative selected area diffraction patterns at each poling field are shown in the insets.

The domain configuration in the left part of the grain shown in Fig. 3(b) was further analyzed. This area contains two sets of edge-on lamellar domains with an intersecting line along the [010] direction, see Fig. 4(a) for an enlarged view. One plausible interpretation is that they are two sets of 120° domains of the orthorhombic phase, and the [010] intersecting line is constructed of alternating 90° and 180° domain wall segments (Fig. 4(b)). Since 180° domain walls usually display extremely weak contrast under TEM, the intersecting line appears discontinuous in the bright field images.

To analyze the domain configurations, charge neutral domain walls are assumed to simplify the process.[34,35] Four essentially different domain walls with spontaneous polarization ($\boldsymbol{P_s}$) subtending angles of 60°, 90°, 120° and 180° can be adopted in the orthorhombic phase, while only 90° and 180° types exist in the tetragonal phase. These ferroelectric domain walls are limited to {100} planes for orthorhombic 90° domains and {110} for both orthorhombic 120° and tetragonal 90° domains. The 180° domain walls for both structures are required only to be parallel to the respective $\boldsymbol{P_s}$ and do not have to be on a specific crystallographic plane. The $\{12\bar{1}\}$ domain walls observed in the two grains along the [111] and [110] zone axes are most likely the orthorhombic 60° domain walls. The curved and inclined boundaries roughly along (011) and (101) planes observed in Figs. 3(c)–3(e) could be domain walls of the monoclinic phase, which will be discussed in more detail later.

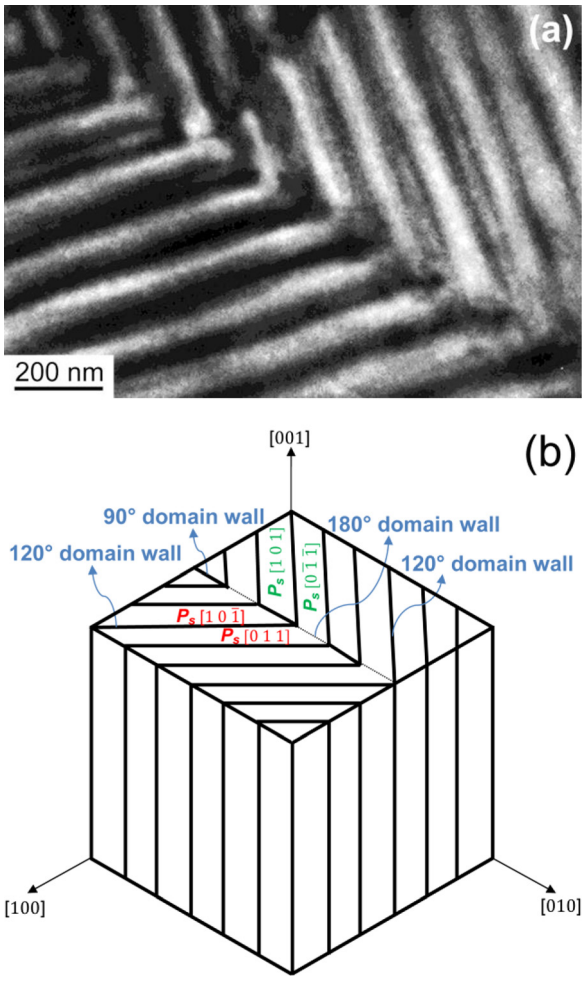

FIG. 4. Interpretation of the orthorhombic structure observed in the left part of the [001]-aligned grain shown in Fig. 3(b). (a) The close-up view of the domain configuration. (b) A schematic illustration of the domains patterns. The polarization vectors $\boldsymbol{P_s}$ of the adjacent four domains are indexed, and associated domain walls are labeled.

In summary, the *in situ* TEM results confirm the existence of the characteristic herringbone domains in the virgin state. These domains transform to thin and long lamellar domains around 8 kV/cm, and then are disrupted and replaced by the blotchy domains at 14 kV/cm and beyond. The blotchy domains are accompanied by the 1/2{*oeo*} superlattice diffraction spots, which are related to electric field-induced oxygen octahedral tilting. All of these microstructural changes under poling fields were found to remain unchanged in TEM at least 30 min after the applied field was removed; the domain morphology alteration and crystal structure transition under poling is an irreversible process in KNN-5.2LS.

B. *Ex situ* X-ray diffraction measurements

The appearance of 1/2{*oeo*} superlattice diffraction during poling was not reported in previous X-ray diffraction experiments on bulk KNN-based PPB compositions.[21–23] *Ex situ* X-ray diffraction is employed on the bulk specimen to verify the appearance of 1/2{*oeo*} superlattice spots observed in the *in situ* TEM experiments. The whole spectra before and after poling are first shown in Fig. 5(a). In the virgin state, the coexistence of the orthorhombic and tetragonal phases is demonstrated by the similar intensities of the (002) and (200) peaks.[15] The peak intensity ratio (I_{002}/I_{200}) is expected to be 2:1 for the pure orthorhombic phase and 1:2 for the pure tetragonal phase.[15] After poling at 30 kV/cm, the relative peak intensities have been obviously changed, especially for the Bragg peaks between 40° and 60° in 2θ. The changes can be attributed to electric field-induced phase transitions as well as the development of a texture due to domain switching.

The development of the 1/2(103) superlattice peak at ~35.3° in the bulk specimen was monitored to verify the appearance of the 1/2{*oeo*} superlattice spots observed in the *in situ* TEM experiments. Fig. 5(b) shows the *ex situ* X-ray diffraction results after poling at a series of electric fields. As can be seen, no superlattice diffraction peak is observed in the virgin state or after poling at 8 kV/cm. The 1/2(103) peak appears at 14 kV/cm and gets slightly stronger at 30 kV/cm. Therefore, the *ex situ* X-ray diffraction measurements on a bulk specimen match exactly with the *in situ* TEM results from a thin foil specimen. In addition, the X-ray diffraction measurements also confirm the irreversibility of the microstructural evolution demonstrated by the *in situ* TEM study.

The 1/2{*oeo*} superlattice diffraction peaks were recently reported in the refined $(1\text{-}x)NaNbO_3$–$xKNbO_3$ binary phase diagram.[36,37] They originated from the $a^0b^+c^0$ oxygen octahedra tilting in the monoclinic space group *Pm*. At 25 °C, this monoclinic phase is stable in the composition range of $0.25 < x < 0.40$. However, according to Glazer[38] and Reaney *et al.*,[33,39] the b^+ in-phase tilting should produce 1/2{*oeo*} superlattice spots with $h \neq l$ (h and l are the two odd Miller indices). This implies that they should be absent

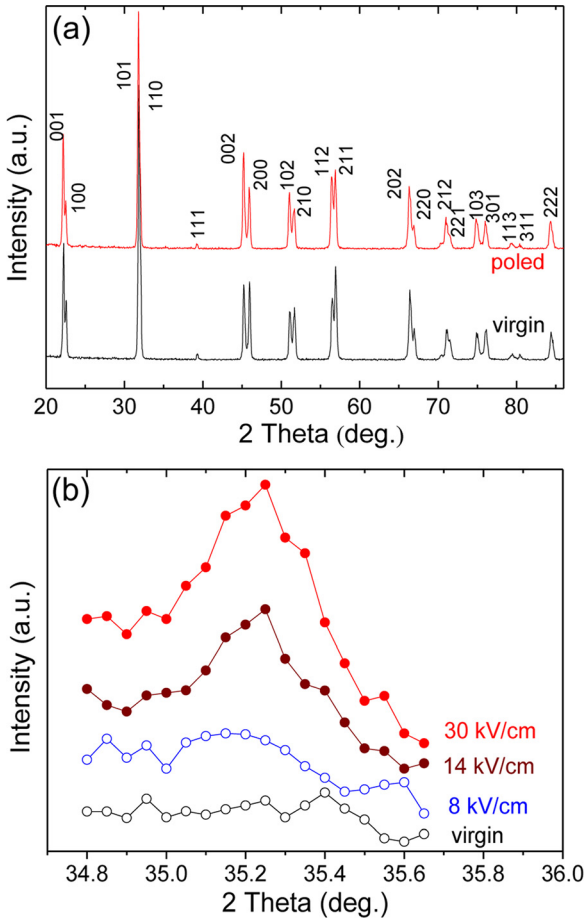

FIG. 5. *Ex situ* X-ray diffraction spectra of a bulk KNN-5.2LS disk poled at different fields. (a) The full spectra in the virgin state and after poling at 30 kV/cm. The peaks are indexed according to a tetragonal unit cell. (b) The profiles with extended data recording time on the same bulk disk reveal the development of the 1/2(103) superlattice peak under electrical poling.

in the ⟨110⟩ zone-axis electron diffraction patterns. The experimentally observed 1/2{*oeo*} superlattice spots in ⟨110⟩ zone-axis patterns in lead zirconate titanate ceramics were hence attributed to antiparallel cation displacements.[40] They occur in the compositionally induced low-symmetry intermediate structures as a result of the frustrated competition between displacive variants with different polarization vectors.[41] In $K_{0.26}Na_{0.74}NbO_3$ at room temperature, Baker *et al.*[37] showed a 1/2(323) superlattice peak (where $h = l$) in the X-ray diffraction data and described the *Pm* monoclinic phase with both $a^0b^+c^0$ tilting and cation displacements order. Therefore, the appearance of the 1/2{*oeo*} diffraction spots in both [111] and [110] zone axes at 14 kV/cm in KNN-5.2LS is due to an electric field-induced phase transition from the orthorhombic *Amm2* phase, which has no oxygen octahedra tilting, to the monoclinic *Pm* phase with $a^0b^+c^0$ tilting, combined with antiparallel cation displacements. At fields of 8 kV/cm and lower, there is domain switching and very likely a small extent of phase transition from tetragonal *P4mm* to orthorhombic *Amm2*.

C. Macroscopic properties

In order to correlate the microstructural changes during poling to macroscopic properties, the dielectric and piezoelectric properties were measured on bulk specimens after poling at a series of fields. The temperature dependent dielectric constant of the bulk sample, poled at a series of fields, is shown in Fig. 6. The measurements were conducted for heating and cooling separately, both starting from room temperature. As reported before, the phase transition temperature between orthorhombic and tetragonal phases ($T_{O\text{-}T}$) of virgin state KNN-5.2LS is around room temperature.[17,18] This is verified again in Fig. 6 as a hump on the dielectric constant curve right at room temperature. Compared with the virgin state, the sample after poling at 8 kV/cm displays a diminished dielectric constant around room temperature, and the hump marking the $T_{O\text{-}T}$ is broadened and appears to be shifted to between 40 °C and 60 °C. Both facts may find microstructural origin from the *in situ* TEM results indicating some extent of tetragonal to orthorhombic phase transition. After poling at 14 and 30 kV/cm, the sample shows a higher dielectric constant around room temperature but decreases much faster during cooling. When heated, a distinct peak with significantly increased values of dielectric constant is observed around 45 °C. This dielectric peak is apparently associated with the poling-induced *Pm* monoclinic phase revealed by the *in situ* TEM and the *ex situ* X-ray diffraction experiments. It indicates the thermally induced monoclinic *Pm* to tetragonal *P4mm* phase transition, and hence the temperature of the transition is denoted $T_{M\text{-}T}$.

The corresponding piezoelectric evolution is shown in Fig. 7, where the piezoelectric coefficient (d_{33}) is plotted as a function of poling field. Three stages can be identified that correlate perfectly with the *in situ* TEM results. In stage I, the poling field is very low and only minimum d_{33} values are measured. Microscopically, the original herringbone type of domain morphology largely remains because almost no domain switching occurs. In stage II, moderate d_{33} values develop due to the herringbone domains being replaced by the lamellar domains via domain switching and phase transition. Stage III, which starts at 14 kV/cm, demonstrates a sudden jump in d_{33} to 237 pC/N. This is induced by the orthorhombic to monoclinic phase transition. Increasing the poling field further only results in a modest change in the d_{33} and finally saturates at 265 pC/N. Hence, the excellent piezoelectric

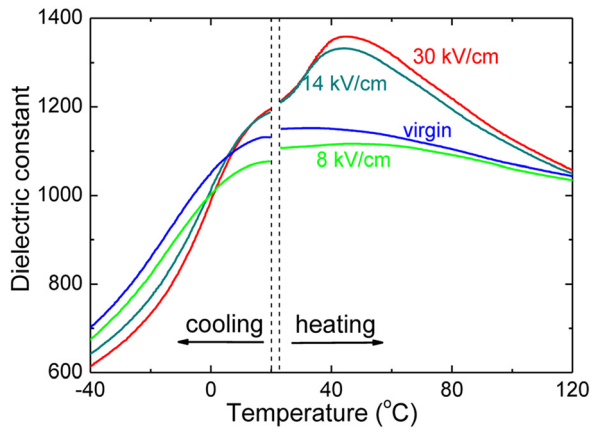

FIG. 6. Temperature dependence of the dielectric constant measured at 10 kHz during heating and cooling on a bulk disk of KNN-5.2LS after poling at a series of electric fields.

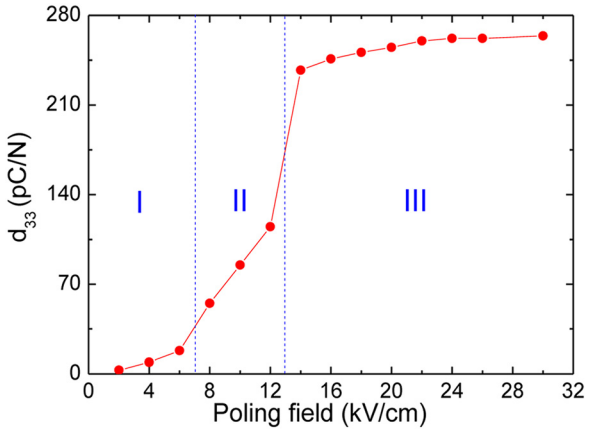

FIG. 7. The development of piezoelectricity, as expressed by the coefficient d_{33}, under electrical poling in a bulk KNN-5.2LS disk.

response of KNN-5.2LS is attributed to the poling-induced monoclinic *Pm* phase with $a^0b^+c^0$ oxygen octahedra tilting and antiparallel cation displacements.

With these experimental results, we can now address the questions raised in the beginning. First, the *Amm2*/*P4mm* PPB is not stable against poling. Poling-induced phase transitions destroy the PPB and eventually form a single phase with the *Pm* space group. This is quite similar to $(1-x)$BNT–xBT with $x=5.5\%$ and $x=6\%$, where the *R3c*/*P4bm* MPB is destroyed and the single phase *R3c* survives the high poling field.[24] Second, the KNN-5.2LS ceramic is extremely responsive to the poling field; complicated domain switching and phase transitions are observed to occur. In addition, dislocation activities seem to participate in the deformation process during electrical poling (Figs. 1(f) and 1(g)). Third, the macroscopic properties correlate very well with the microstructural evolution during poling. The microstructural mechanism for the enhanced piezoelectricity is the presence of the tilted *Pm* phase after poling. The large number of equivalent polar axis (24) in the monoclinic phase (for comparison, 6 in tetragonal and 12 in orthorhombic) makes the poling easier and more thorough. Of course, the close-to-room-temperature phase transition ($T_{\text{M-T}}\sim 45\,^{\circ}\text{C}$) provides the necessary structural instability. Apparently, this mechanism is quite different from that of $(1-x)$BNT–xBT. For $x=7\%$, the composition with the best d_{33} value, an *R3c*/*P4mm* MPB is created from the original *P4bm* single phase by poling and is responsible for the enhanced piezoelectricity.[24] Finally, we argue that even though the *Amm2*/*P4mm* PPB in KNN-5.2LS does not exist after poling, it is still important to the enhanced piezoelectric response. The existence of the PPB at room temperature indicates that multiple ferroelectric phases with varied distortions have similar free energies at this temperature. This guarantees easy electric field-induced phase transitions, which allows the transformation to the monoclinic phase during poling.

The discovery presented here will be helpful to the development of lead-free piezoelectric ceramics. It demonstrates the importance of the structural instability associated with either PPB or MPB to the piezoelectric property. The coexistence of multiple phases is a sign of comparable free energies and guarantees the involvement of phase transitions during piezoelectric activities under electric fields or mechanical stresses. In addition, the strong competition between the coexisting ferroelectric phases may also result in low-symmetry structures, and this process can be assisted by external stimuli. As proven here in the KNN-5.2LS ceramic, poling fields assisted the formation of the *Pm* structure due to the competition between the orthorhombic phase with the ⟨110⟩ polarization and the tetragonal phase with the ⟨001⟩ polarization. It is also very interesting to notice that once a stable low-symmetry phase is resulted from the competition, excellent piezoelectric properties ensue. This is the case here; this is the case in lead zirconate titanate.[40,42]

IV. CONCLUSIONS

An electric field *in situ* TEM study was conducted for the first time on an archetypical KNN-based lead-free piezoelectrics: the polymorphic phase boundary composition KNN-5.2LS. It is found that the original herringbone domain patterns of mixed tetragonal and orthorhombic phases change to thin lamellar domains when the poling field reaches 8 kV/cm. This process involves domain switching as well as some extent of tetragonal to orthorhombic phase transition. At 14 kV/cm, a monoclinic *Pm* phase with $a^0b^+c^0$ oxygen octahedra tilting and antiparallel cation displacements forms, as manifested by the appearance of blotchy domains and 1/2{*oeo*} superlattice diffraction spots. These microstructural changes in response to electrical poling fields remain after the field is removed; therefore, they determine the macroscopic properties of poled ceramics. The poling-induced monoclinic phase and its low transition temperature ($T_{\text{M-T}}$) are responsible for the enhanced piezoelectric response of this ceramic. The microscopic structure and macroscopic property relationship elucidated here not only explains the KNN-5.2LS but will hopefully allow for the identification of new compositions that will assist in the development of lead-free piezoelectrics.

ACKNOWLEDGMENTS

X.T. acknowledges Dr. Ian Reaney and Dr. Jacob Jones for their critical review and helpful discussion. The National Science Foundation (NSF), through Grant No. DMR-1037898, supported this work. TEM experiments were performed at the Ames Laboratory, which is operated for the U.S. DOE by Iowa State University under Contract No. DE-AC02-07CH11358.

[1]B. Jaffe, R. S. Roth, and S. Marzullo, J. Appl. Phys. **25**, 809 (1954).
[2]D. Damjanovic, J. Appl. Phys. **82**, 1788 (1997).
[3]B. Jaffe, W. R. Cook, and H. Jaffe, *Piezoelectric Ceramics* (Academic Press, London, 1971).
[4]J. Rödel, W. Jo, K. Seifert, E. M. Anton, T. Granzow, and D. Damjanovic, J. Am. Ceram. Soc. **92**, 1153 (2009).
[5]T. R. Shrout and S. J. Zhang, J. Electroceram. **19**, 113 (2007).
[6]L. Egerton and D. M. Dillon, J. Am. Ceram. Soc. **42**, 438 (1959).
[7]R. E. Jaeger and L. Egerton, J. Am. Ceram. Soc. **45**, 209 (1962).
[8]Y. Satio, H. Takao, T. Tani, T. Nonoyama, K. Takatori, T. Homma, T. Nagaya, and M. Nakamura, Nature **432**, 84 (2004).
[9]M. Suewattana and D. J. Singh, Phys. Rev. B **82**, 014114 (2010).

[10]M. Abazari and A. Safari, J. Appl. Phys. **105**, 094101 (2009).
[11]W. Ge, Y. Ren, J. Zhang, C. P. Devreugd, J. Li, and D. Viehland, J. Appl. Phys. **111**, 103503 (2012).
[12]E. Hollenstein, M. Davis, D. Damjanovic, and N. Setter, Appl. Phys. Lett. **87**, 182905 (2005).
[13]Y. P. Guo, K. Kakimoto, and H. Ohsato, Mater. Lett. **59**, 241 (2005).
[14]Y. P. Guo, K. Kakimoto, and H. Ohsato, Appl. Phys. Lett. **85**, 4121 (2004).
[15]K. Wang and J. F. Li, Adv. Funct. Mater. **20**, 1924 (2010).
[16]K. Wang and J. F. Li, Appl. Phys. Lett. **91**, 262902 (2007).
[17]S. J. Zhang, R. Xia, T. R. Shrout, G. Z. Zang, and J. F. Wang, J. Appl. Phys. **100**, 104108 (2006).
[18]S. J. Zhang, R. Xia, T. R. Shrout, G. Z. Zang, and J. F. Wang, Solid State Commun. **141**, 675 (2007).
[19]J. Fu, R. Z. Zuo, and Z. K. Xu, Appl. Phys. Lett. **99**, 062901 (2011).
[20]W. G. Cady, *Piezoelectricity* (McGraw-Hill, New York, 1946).
[21]W. W. Ge, J. F. Li, D. Viehland, Y. F. Chang, and G. L. Messing, Phys. Rev. B **83**, 224110 (2011).
[22]J. Fu, R. Z. Zuo, S. C. Wu, J. Z. Jiang, L. Li, T. Y. Yang, X. H. Wang, and L. T. Li, Appl. Phys. Lett. **100**, 122902 (2012).
[23]R. Z. Zuo, J. Fu, G. Z. Yin, X. L. Li, and J. Z. Jiang, Appl. Phys. Lett. **101**, 092906 (2012).
[24]C. Ma, H. Z. Guo, S. P. Beckman, and X. Tan, Phys. Rev. Lett. **109**, 107602 (2012).
[25]X. Tan, Z. Xu, J. K. Shang, and P. Han, Appl. Phys. Lett. **77**, 1529 (2000).
[26]H. Z. Guo, C. Ma, X. M. Liu, and X. Tan, Appl. Phys. Lett. **102**, 092902 (2013).
[27]X. Tan, H. He, and J. K. Shang, J. Mater. Res. **20**, 1641 (2005).
[28]H. He and X. Tan, Phys. Rev. B **72**, 024102 (2005).
[29]X. Tan and J. K. Shang, Philos. Mag. A **82**, 1463 (2002).
[30]G. Arlt and P. Sasko, J. Appl. Phys. **51**, 4956 (1980).
[31]R. López-Juárez, O. Novelo-Peralta, F. González-García, F. Rubio-Marcos, and M.-E. Villafuerte-Castrejón, J. Eur. Ceram. Soc. **31**, 1861 (2011).
[32]R. P. Herber, G. A. Schneider, S. Wagner, and M. J. Hoffmann, Appl. Phys. Lett. **90**, 252905 (2007).
[33]D. I. Woodward and I. M. Reaney, Acta Cryst. B **61**, 387 (2005).
[34]E. Wiesendanger, Czech. J. Phys. B **23**, 91 (1973).
[35]J. Hirohashi, K. Yamada, H. Kamio, M. Uchida, and S. Shichijyo, J. Appl. Phys. **98**, 034107 (2005).
[36]D. W. Baker, P. A. Thomas, N. Zhang, and A. M. Glazer, Appl. Phys. Lett. **95**, 091903 (2009).
[37]D. W. Baker, P. A. Thomas, N. Zhang, and A. M. Glazer, Acta Cryst. B **65**, 22 (2009).
[38]A. M. Glazer, Acta Cryst. A **31**, 756 (1975).
[39]I. M. Reaney, E. L. Colla, and N. Setter, Jpn. J. Appl. Phys. **33**, 3984 (1994).
[40]D. I. Woodward, J. Knudsen, and I. M. Reaney, Phys. Rev. B **72**, 104110 (2005).
[41]I. M. Reaney, D. I. Woodward, and C. A. Randall, J. Am. Ceram. Soc. **94**, 2242 (2011).
[42]B. Noheda, D. E. Cox, G. Shirane, J. A. Gonzalo, L. E. Cross, and S. E. Park, Appl. Phys. Lett. **74**, 2059 (1999).